Systematic mapping of the state dependence of voltage- and Ca^{2+}-dependent inactivation using simple open-channel measurements

Michael R. Tadross[2] and David T. Yue[1,2]

[1]Department of Neuroscience and [2]Department of Biomedical Engineering, The Johns Hopkins University School of Medicine, Baltimore, MD 21205

The state from which channel inactivation occurs is both biologically and mechanistically critical. For example, preferential closed-state inactivation is potentiated in certain Ca^{2+} channel splice variants, yielding an enhancement of inactivation during action potential trains, which has important consequences for short-term synaptic plasticity. Mechanistically, the structural substrates of inactivation are now being resolved, yielding a growing library of molecular snapshots, ripe for functional interpretation. For these reasons, there is an increasing need for experimentally direct and systematic means of determining the states from which inactivation proceeds. Although many approaches have been devised, most rely upon numerical models that require detailed knowledge of channel-state topology and gating parameters. Moreover, prior strategies have only addressed voltage-dependent forms of inactivation (VDI), and have not been readily applicable to Ca^{2+}-dependent inactivation (CDI), a vital form of regulation in numerous contexts. Here, we devise a simple yet systematic approach, applicable to both VDI and CDI, for semiquantitative mapping of the states from which inactivation occurs, based only on open-channel measurements. The method is relatively insensitive to the specifics of channel gating and does not require detailed knowledge of state topology or gating parameters. Rather than numerical models, we derive analytic equations that permit determination of the states from which inactivation occurs, based on direct manipulation of data. We apply this methodology to both VDI and CDI of $Ca_V1.3$ Ca^{2+} channels. VDI is found to proceed almost exclusively from the open state. CDI proceeds equally from the open and nearby closed states, but is disfavored from deep closed states distant from the open conformation. In all, these outcomes substantiate and enrich conclusions of our companion paper in this issue (Tadross et al. 2010. *J. Gen. Physiol.* doi:10.1085/jgp.200910308) that deduces endpoint mechanisms of VDI and CDI in $Ca_V1.3$. More broadly, the methods introduced herein can be readily generalized for the analysis of other channel types.

The Journal of General Physiology

INTRODUCTION

In the earliest conceptions of voltage-gated channels, inactivation of Na^+ channels was thought to proceed equally from all noninactivated channel conformations, and transitions leading to inactivation were believed intrinsically voltage dependent (Hodgkin and Huxley, 1952). With measurements of increasing resolution, however, many voltage-dependent inactivation (VDI) processes were seen to proceed preferentially from the open conformation, with little genuine voltage dependence attributable to actual transitions into inactivated states in Na^+ and K^+ channels (Armstrong and Bezanilla, 1977; Bean, 1981; Aldrich et al., 1983; Bezanilla and Stefani, 1994; Zagotta et al., 1994). Moreover, notable variations on this theme have been observed in certain K^+ channels, where VDI proceeds preferentially from intermediate closed states in the activation pathway (Aldrich, 1981; Klemic et al., 1998). Similarly, such preferential closed-state inactivation can also be detected in neuronal Ca_V2 Ca^{2+} channels that are comprised of certain auxiliary subunits (Jones et al., 1999; Patil et al., 1998) and splice variations (Thaler et al., 2004). These latter case examples of preferential closed-state inactivation amplify the inactivation seen upon neuronal spike activation, compared with the square-pulse depolarization commonly used in biophysical analysis. Accordingly, such closed-state inactivation in Ca^{2+} channels holds important consequences for short-term synaptic plasticity (Patil et al., 1998; Thaler et al., 2004; Xu and Wu, 2005).

Growing awareness of these biological implications, along with the emergence of x-ray structures that could establish an atomic view of inactivation (MacKinnon, 2003; Cuello et al., 2009), heightens the motivation for improved methodologies to ascertain preferred pathways into inactivation. Although such methodologies exist, as exemplified in the aforementioned references, the task can be inherently challenging, as the most

Correspondence to David T. Yue: dyue@jhmi.edu; or Michael R. Tadross: mtadross@gmail.com

Abbreviations used in this paper: apoCaM, Ca^{2+}-free calmodulin; CaM, calmodulin; CDI, Ca^{2+}-dependent inactivation; VDI, voltage-dependent inactivation.

© 2010 Tadross and Yue This article is distributed under the terms of an Attribution–Noncommercial–Share Alike–No Mirror Sites license for the first six months after the publication date (see http://www.rupress.org/terms). After six months it is available under a Creative Commons License (Attribution–Noncommercial–Share Alike 3.0 Unported license, as described at http://creativecommons.org/licenses/by-nc-sa/3.0/).

The Rockefeller University Press $30.00
J. Gen. Physiol. Vol. 135 No. 3 217–227
www.jgp.org/cgi/doi/10.1085/jgp.200910309

direct measurements are of ionic current through the open conformation, whereas the closed states leading to inactivation and inactivation itself are inherently nonconducting, and thereby one or more steps removed from direct observation. Moreover, the existing methodologies are often numerical modeling intensive and require detailed knowledge of the gating structure of specific channels in question. Finally, none of the present strategies addresses a different but important class of inactivation, that driven by intracellular Ca^{2+} (Brehm and Eckert, 1978). Such Ca^{2+}-dependent inactivation (CDI) furnishes a critical form of Ca^{2+} feedback, wherein certain transitions leading to inactivation are inherently Ca^{2+} dependent.

Nowhere are these methodological deficits more apparent than in the setting of voltage-gated Ca^{2+} channels, which manifest both VDI and CDI. Due to longstanding technical challenges in the study of these channels, such as limited expression levels and channel rundown upon patch excision (Wu et al., 2002), in-depth knowledge of gating kinetics is more limited here than in voltage-gated K^+ and Na^+ channels. Here, we therefore devise a simple, yet systematic strategy for determining preferred pathways into VDI and CDI, based only upon readily accessible open-channel measurements. The method makes few assumptions about the gating scheme of the channel in question, allows for direct analytic manipulation of experimental data, and circumvents the need for detailed numerical modeling. For VDI, the technique only requires knowledge of steady-state inactivation as a function of voltage. In the case of CDI, single-channel open probability, unitary current amplitude, and whole cell "voltage block" experiments (Tadross et al., 2008) are additionally required. From these data, we can furnish semiquantitative mapping of the states from which inactivation occurs. We apply this methodology to the inactivation of $Ca_V1.3$ Ca^{2+} channels, the subject of investigation in our companion paper (see Tadross et al. in this issue). In these channels, VDI is seen to proceed almost exclusively from the open state. CDI paints a somewhat different picture, proceeding equally from the open and nearby closed states, while proceeding less well from closed states more distant from the open conformation. All of these particular outcomes strengthen the mechanistic deductions of our companion paper, which concern the end points of $Ca_V1.3$ inactivation. Viewed from a wider perspective, our methodologies represent general tools applicable to the analysis of many other types of channels.

MATERIALS AND METHODS

HEK293 cells were cultured, maintained, and transfected with $Ca_V1.3$ channel subunits as described in our companion paper (Tadross et al., 2010). Whole cell recording methodology and analysis were also as described in that publication. Single-channel data are reproduced from prior work (Tadross et al., 2008), which contains detailed single-channel methodology.

RESULTS AND DISCUSSION

General formulation of activation and inactivation at equilibrium

As a prelude to the upcoming analysis, we found it useful to cast the standard equilibrium expressions for activation and inactivation in a compact and general format. To start, Fig. 1 A illustrates a familiar multistate gating scheme featuring voltage-dependent transitions between numerous closed states and a single open state. The voltage-dependent equilibria between states in the top row are given by $Q(V)$ and $L(V)$. For example, $Q_1(V)$ specifies the ratio of state C_2 to state C_1 occupancy at equilibrium, and so forth. Likewise, inactivation may occur from any of the states in the top row, according to equilibrium constants $J_{C1}, J_{C2}, \ldots, J_O$. As well, no explicit interconnections are drawn between inactivated states because equilibria between these states would already be specified by the parameters shown, according to the dictates of thermodynamic cycles. Although we show four closed states, the actual number of closed states could be increased or decreased without affecting our upcoming analysis. Moreover, no restrictions are imposed upon the voltage-dependent equilibrium constants $Q(V)$ and $L(V)$; they can bear a standard single-exponential dependence on voltage, or they can be arbitrarily complex functions of voltage. To facilitate interpretation of the final result, the inactivation equilibrium constants ($J_{C1}, J_{C2}, \ldots, J_O$) are taken to be voltage independent; however, the methodology is still applicable if this condition is relaxed.

Given that activation usually occurs much faster than inactivation, mainly states in the top row are occupied during the first few milliseconds of depolarization, so the approximate probability of occupying each state during this time window would be:

$$P_{C1}(V) = \frac{1}{1 + Q_1 + Q_1 \cdot Q_2 + Q_1 \cdot Q_2 \cdot Q_3 + Q_1 \cdot Q_2 \cdot Q_3 \cdot L} \quad (1)$$

$$P_{C2}(V) = \frac{Q_1}{1 + Q_1 + Q_1 \cdot Q_2 + Q_1 \cdot Q_2 \cdot Q_3 + Q_1 \cdot Q_2 \cdot Q_3 \cdot L}$$

$$P_{C3}(V) = \frac{Q_1 \cdot Q_2}{1 + Q_1 + Q_1 \cdot Q_2 + Q_1 \cdot Q_2 \cdot Q_3 + Q_1 \cdot Q_2 \cdot Q_3 \cdot L}$$

$$P_{C4}(V) = \frac{Q_1 \cdot Q_2 \cdot Q_3}{1 + Q_1 + Q_1 \cdot Q_2 + Q_1 \cdot Q_2 \cdot Q_3 + Q_1 \cdot Q_2 \cdot Q_3 \cdot L}$$

$$P_O(V) = \frac{Q_1 \cdot Q_2 \cdot Q_3 \cdot L}{1 + Q_1 + Q_1 \cdot Q_2 + Q_1 \cdot Q_2 \cdot Q_3 + Q_1 \cdot Q_2 \cdot Q_3 \cdot L}$$

These are steady-state probabilities in the absence of inactivation. After some time, inactivated states also

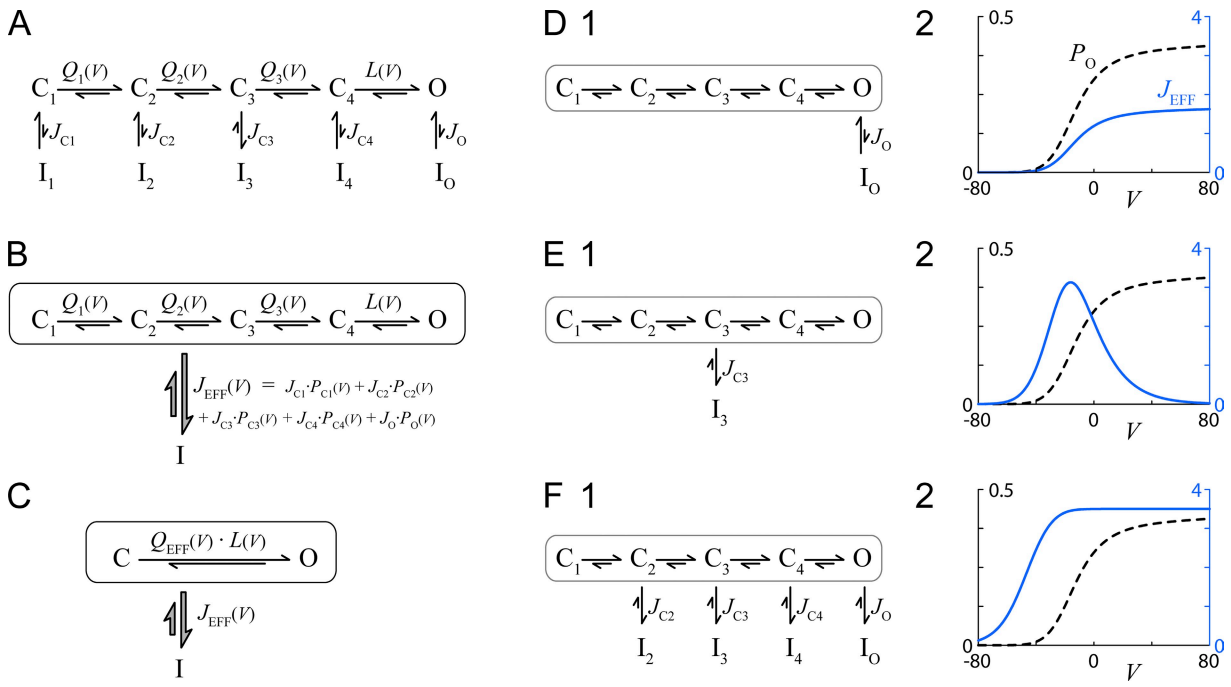

Figure 1. VDI analysis for detailed, multistate gating diagram. (A) Channel activation involves numerous closed states, with a single open state (top row). Inactivation (bottom row) can occur from any or all of the states in the top row. Equilibrium constants are as shown. (B and C) Simplified but equivalent state diagrams. (D) Behavior of the model in A if inactivation were to proceed exclusively from the open conformation. (D, 2) P_O (Eq. 1) and J_{EFF} (Eq. 3) as functions of V (mV). Parameters are as follows: $Q_1(V) = 40 \cdot \exp(0.1 \cdot (V+10))$, $Q_2(V) = 20 \cdot \exp(0.08 \cdot (V-22.9))$, $Q_3(V) = 10 \cdot \exp(0.06 \cdot (V-21.9))$, $L(V) = 0.659 \cdot \exp(0.001 \cdot (V-41))$, $J_{C1} = J_{C2} = J_{C3} = J_{C4} = 0$, and $J_O = 4$. (E) Behavior of the model in A if inactivation were to proceed exclusively from state C_3. Format and parameters identical to D, except $J_{C1} = J_{C2} = J_{C4} = J_O = 0$ and $J_{C3} = 12$. (F) Behavior of the model in A if inactivation were to proceed equally from states C_2, C_3, C_4, and O. Format and parameters as in D, except $J_{C1} = 0$ and $J_{C2} = J_{C3} = J_{C4} = J_O = 3.5$.

become occupied, yielding an equilibrium open probability:

$$P_{O,SS}(V) = \frac{Q_1 \cdot Q_2 \cdot Q_3 \cdot L}{\begin{pmatrix} 1 & +Q_1 & +Q_1 \cdot Q_2 & +Q_1 \cdot Q_2 \cdot Q_3 & +Q_1 \cdot Q_2 \cdot Q_3 \cdot L & + \\ J_{C1} & +Q_1 \cdot J_{C2} & +Q_1 \cdot Q_2 \cdot J_{C3} & +Q_1 \cdot Q_2 \cdot Q_3 \cdot J_{C4} & +Q_1 \cdot Q_2 \cdot Q_3 \cdot L \cdot J_O & \end{pmatrix}} \quad (2)$$

Next, we consider two simplifications. First, without any assumptions on the parameters of Fig. 1 A, we can recapitulate the behavior of this state diagram using a simpler but equivalent scheme, shown in Fig. 1 B. Here, the top and bottom rows become single aggregate states, interconnected by a single "effective" equilibrium constant J_{EFF}, which is equal to the weighted sum of individual J factors. Importantly, the weighting factors are the steady-state probabilities of occupying various states in the top row, given residence in the top row.

$$J_{EFF}(V) = J_{C1} \cdot P_{C1}(V) + J_{C2} \cdot P_{C2}(V) + J_{C3} \cdot P_{C3}(V) + J_{C4} \cdot P_{C4}(V) + J_O \cdot P_O(V) = \sum_{k \in \left[\begin{smallmatrix}\text{gating state}\\ \text{in upper row}\end{smallmatrix}\right]} J_{\left[\begin{smallmatrix}\text{inactivation}\\ \text{constant}\\ \text{from state } k\end{smallmatrix}\right]} \times P_{\left[\begin{smallmatrix}\text{occupancy}\\ \text{of state } k \text{ given}\\ \text{upper row residence}\end{smallmatrix}\right]}(V) \quad (3)$$

Second, the system in Fig. 1 B can be further simplified into the system shown in Fig. 1 C, as follows. We start by reorganizing $P_O(V)$ from Eq. 1 into

$$P_O(V) = \frac{\frac{Q_1 \cdot Q_2 \cdot Q_3}{1 + Q_1 + Q_1 \cdot Q_2 + Q_1 \cdot Q_2 \cdot Q_3} \cdot L}{1 + \frac{Q_1 \cdot Q_2 \cdot Q_3}{1 + Q_1 + Q_1 \cdot Q_2 + Q_1 \cdot Q_2 \cdot Q_3} \cdot L} \quad (4)$$

It now becomes natural to define:

$$Q_{EFF}(V) = \frac{Q_1 \cdot Q_2 \cdot Q_3}{1 + Q_1 + Q_1 \cdot Q_2 + Q_1 \cdot Q_2 \cdot Q_3} \quad (5)$$

Combining the last two equations yields a modified version of Eq. 1:

$$P_O(V) = \frac{Q_{EFF}(V) \cdot L}{1 + Q_{EFF}(V) \cdot L} \quad (6)$$

Similarly, Eq. 2 can be modified to yield:

$$P_{O,SS}(V) = P_O(V) \cdot \frac{1}{1 + J_{EFF}(V)} \quad (7)$$

Eqs. 6 and 7 describe the activated and steady-state open probability of the most simplified scheme in Fig. 1 C. Because Eqs. 6 and 7 are identical to Eqs. 1 and 2 (derived for Fig. 1 A), all three schemes in Fig. 1 (A–C) must behave identically with regard to peak and steady-state open probabilities. In this sense, all three state diagrams in Fig. 1 (A–C) are equivalent without loss of generality and without any assumptions on the state transition parameters. These different but equivalent diagrams are helpful in our subsequent deliberations.

Pathways to VDI

Given these preliminaries, we turned to the identification of preferred states leading to VDI. As in our companion paper (Tadross et al., 2010), we consider a standard measure of inactivation, the fraction of peak current lost at steady state. From Eqs. 6 and 7, this is given by:

$$VDI(V) = \frac{P_O(V) - P_{O,SS}(V)}{P_O(V)} = \frac{J_{EFF}(V)}{1 + J_{EFF}(V)} \quad (8)$$

Because *VDI* is completely determined by J_{EFF}, we can invert this relation as follows:

$$J_{EFF}(V) = \frac{VDI(V)}{1 - VDI(V)} \quad (9)$$

Eq. 9 yields a very useful and simple result. It enables us to calculate $J_{EFF}(V)$ based upon readily obtained experimental measurements of $VDI(V)$. Moreover, it can be shown that Eq. 9 holds for considerably more complex models of channel gating. For example, even if gating involved N (arbitrary number) of closed states, Eq. 9 would still hold, with $J_{EFF}(V)$ consisting of $N+1$ terms, as described by Eq. 3.

From the voltage dependence of $J_{EFF}(V)$, we can determine whether inactivation occurs preferentially from certain states along the activation pathway, as illustrated in Fig. 1 (D–F). First, if inactivation were to proceed exclusively from the open state (as diagrammed in Fig. 1 D, 1), $J_{EFF}(V)$ would rise with increasing voltage (blue curve in Fig. 1 D, 2), mirroring $P_O(V)$ (dashed curve). In contrast, for inactivation that proceeds exclusively from an intermediate closed state (e.g., state C_3 in Fig. 1 E, 1), $J_{EFF}(V)$ would exhibit a bell-shaped dependence upon V (blue curve in Fig. 1 E, 2), mirroring $P_{C3}(V)$. Finally, if inactivation were to proceed equally from states C_2, C_3, C_4, and O (Fig. 1 F, 1), $J_{EFF}(V)$ would assume the monotonically increasing blue relation in Fig. 1 F (2), which notably rises to the left of channel opening. From these, it is clear that preferential inactivation from closed versus open states could be clearly distinguished. Importantly, all that is needed to determine the state dependence of VDI is Eq. 9 in conjunction with an experimental measure of VDI as a function of depolarization voltage.

Fig. 2 shows the actual analysis applied to experimental data for two $Ca_V1.3$ constructs (D1464P and F1166P) from our companion paper (Tadross et al., 2010). These constructs have been engineered for enhanced VDI, thereby furnishing a robust context for this analysis. In Fig. 2, A and C display the extent of VDI as a function of step potential, and these are transformed via Eq. 9 into the corresponding plots of $J_{EFF}(V)$ (blue relations) shown in B and D. The close similarity of $J_{EFF}(V)$ to the plot of normalized open probability $P_O(V)$ (B and D, black relations and data points reproduced from

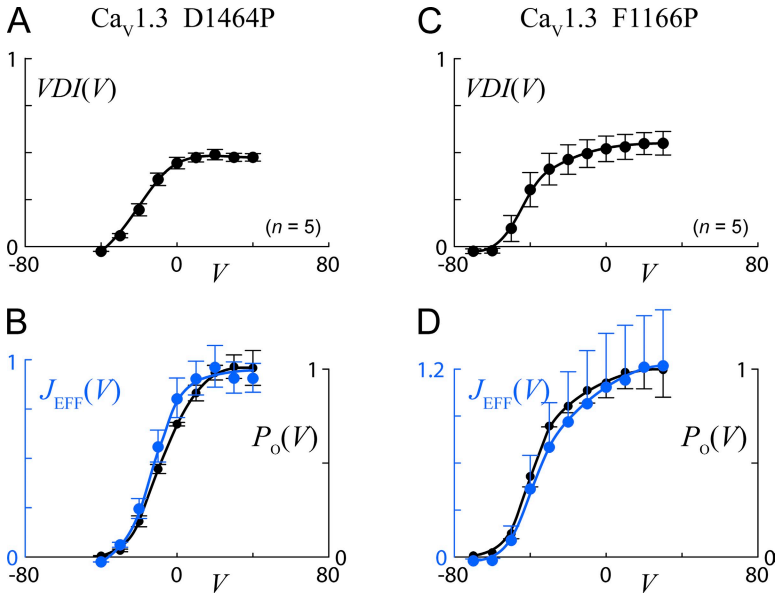

Figure 2. J_{EFF} analysis applied to two $Ca_V1.3$ constructs with enhanced VDI (see our companion paper, Tadross et al., 2010), D1464P (left panels) and F116P (right panels). (A and C) VDI_{300} parameters (see Fig. 2, A and B, of our companion paper [Tadross et al., 2010] for definition) plotted as a function of voltage (mV). Error bars show SEM. Number of cells (n) as indicated. (B and D) Close similarity of J_{EFF} (blue) and normalized $P_O(V)$ (black), arguing for predominance of voltage inactivation from the open state. J_{EFF} is calculated from data in A and C according to Eq. 9, and P_O is the normalized open probability from our companion paper (Tadross et al., 2010), both plotted as a function of voltage (mV). Error bars represent the SEM, as estimated by transforming the mean ± SEM from A and C via Eq. 9.

Tadross et al., 2010) argues that VDI proceeds predominantly from the open state in these channels.

Pathways to CDI

In voltage-gated Ca^{2+} channels, another important form of inactivation is driven by elevations of intracellular Ca^{2+}, rather than depolarization (Evans and Zamponi, 2006; Dunlap, 2007). This CDI furnishes a biologically essential form of activity-dependent regulation. For the majority of Ca^{2+} channels, those in the Ca_V1 and Ca_V2 clades, CDI is mediated by a resident calmodulin (CaM) molecule, which is persistently associated with the channel as a functional channel subunit. In this manner, CaM acts as the Ca^{2+} sensor that triggers CDI in the CaM/channel complex. Despite this added level of complexity, our methodology for extracting the state dependence of CDI will be analogous to the VDI case, with some additional techniques to account explicitly for variable Ca^{2+} entry through channels, which is itself a voltage-dependent process.

As before, our goal will be to derive an analytic expression for $J_{EFF}(V)$ that holds for a broad class of gating models. For this treatment, we consider a generalized gating scheme for CaM-mediated CDI of Ca^{2+} channels (Fig. 3 A), which pertains directly to extensively characterized forms of CDI driven by Ca^{2+} binding to a single lobe of CaM (Tadross et al., 2008). As in the VDI treatment, horizontal transitions represent the voltage-dependent gating steps involved in channel activation, with numerous closed states and a single open state. The additional feature here concerns the extensive system of vertical transitions linking the top four rows, which represent CaM-mediated steps involved in CDI. These four rows are based upon a previously established four-state mechanism of CDI (Tadross et al., 2008). The bottom row (row 5) shows the familiar set of inactivated states, analogous to the VDI case. A cartoon next to each row depicts the essential features of each configuration, as follows. The top row represents Ca^{2+}-free CaM (apoCaM; yellow circle) bound to the channel pre-association site (round pocket). Row 2 portrays apoCaM after it has released from the pre-association site, at which point it can bind Ca^{2+} to produce Ca^{2+}/CaM (square) in row 3. Importantly, it is not until the channel reaches row 4 (where Ca^{2+}/CaM is bound to the channel effector site, shown as a square pocket) that outright CDI may be achieved in row 5. Indeed, rows 4 and 5 are closely analogous to the VDI scheme in Fig. 1 A, where J factors (J_{C1}, J_{C2}, … , J_O) concern the inactivation from various states in row 4.

As for the vertical transitions among rows 1–4, we use a first-order approximation where channel affinity for apoCaM (specified by e and d) and channel affinity for Ca^{2+}/CaM (specified by α and β) are independent of activation gating. Similarly, the CaM affinity for Ca^{2+} (specified by k_{on} and k_{off}) is considered independent of activation. However, because Ca^{2+} entry is coupled to

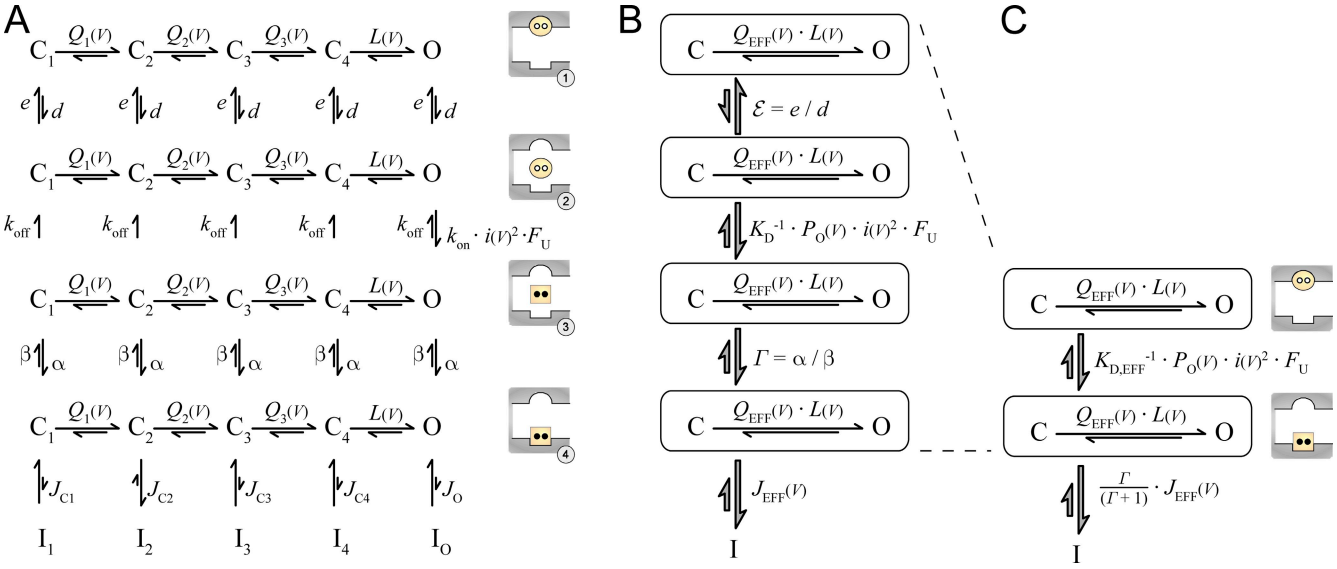

Figure 3. Multistate gating diagram for CDI analysis. (A) Generalized multistate diagram describing CaM-mediated CDI. Horizontal transitions refer to standard channel activation, identical to that in Fig. 1 A. Vertical transitions relate to various steps in the progression to CDI. The top four rows correspond to different CaM/channel configurations, and the physical significance of each configuration is cartooned to the right of each row. In row 1, apoCaM (yellow circle) is bound to the apoCaM site (round pocket). In row 2, apoCaM has transiently dissociated from the channel. In row 3, CaM has bound two Ca^{2+} ions (black dots) to become Ca^{2+}/CaM (yellow square), which then binds the Ca^{2+}/CaM effector site (square pocket) in row 4. Channels in row 4 are primed for inactivation and can become inactivated according to state-dependent equilibrium constants, analogous to those in Fig. 1 A. (B and C) Simplified but equivalent state diagrams, assuming the slow CaM regimen. In B, $K_D = k_{off}/k_{on}$ is the Ca^{2+} dissociation constant of a transiently dissociated CaM (see cartoon of rows 2 and 3). In C, $K_{D,EFF} = K_D \cdot (\varepsilon + 1)/(\Gamma + 1)$ is the effective Ca^{2+} dissociation constant of the entire CaM/channel complex.

channel gating, the downward rate constants between rows 2 and 3 differ for closed versus open states. For closed states, the downward rate constants are set to 0 due to the lack of Ca^{2+} elevation during closures. This is particularly true given our use of high intracellular Ca^{2+} buffering, which eliminates residual Ca^{2+} between openings. In the open conformation, the downward rate constant is equal to $k_{on} \cdot i(V)^2 \cdot F_U$, where k_{on} is in units of $sec^{-1} \cdot pA^{-2}$, and $i(V)$ is the unitary calcium current in the open state, which depends on voltage via a GHK-like relation (Tadross et al., 2008). The squared dependence on unitary current reflects the cooperative binding of two Ca^{2+} ions by a lobe of CaM (Peterson et al., 2000). F_U ("fraction unblocked") is a parameter that becomes relevant during voltage block experiments (Tadross et al., 2008), data from which will be incorporated in our upcoming analysis. During a normal depolarization, $F_U = 1$, indicating that open channels always permeate calcium. During voltage block experiments, $0 < F_U < 1$ because the protocol "chop blocks" Ca^{2+} entry for a fraction of time, even in the open conformation.

Similar to our prior VDI analysis, the scheme in Fig. 3 A can be transformed into compact equivalent forms. Without loss of generality, each row can be converted into an aggregate state wherein horizontal gating transitions are compressed into two-state C↔O schemes, with $Q_{EFF}(V)$ specified by Eq. 5. The resulting rows in Fig. 3 B are now interconnected by effective equilibrium constants, where $\varepsilon = e/d$, $\Gamma = \alpha/\beta$, and J_{EFF} is equal to the weighted sum of individual J factors as specified by Eq. 3. As for the directly Ca^{2+}-driven transitions between rows 2 and 3, an effective equilibrium constant can also be specified so long as k_{off} is slow relative to horizontal gating transitions. This is known as the "slow CaM" condition, which has been shown to predominate in $Ca_V1.3$ channels (Tadross et al., 2008). The resulting equilibrium constant becomes $K_D^{-1} \cdot P_O(V) \cdot i(V)^2 \cdot F_U$, where $K_D = k_{off}/k_{on}$ is the Ca^{2+} dissociation constant of CaM, and $P_O(V)$ is the open probability of noninactivated channels (Eq. 1). Finally, the top four rows of Fig. 3 B, which characterize Ca^{2+} binding by the CaM/channel complex, can be entirely recapitulated by the two-row scheme in Fig. 3 C. In this condensed format, the effective Ca^{2+} dissociation constant, $K_{D,EFF} = K_D \cdot (\varepsilon + 1)/(\Gamma + 1)$, represents the Ca^{2+} dissociation constant of the entire CaM/channel complex. As well, $J_{EFF}(V)$ is nominally scaled by a constant $\Gamma/(\Gamma + 1)$, which is nonetheless ~1 for the usual CDI that nearly achieves completion. In all then, the steady-state behavior of the scheme in Fig. 3 A is equivalent to that in Fig. 3 C, with no assumptions other than the slow CaM condition.

Given this setup, we can deduce that CDI depends on $J_{EFF}(V)$, much as VDI did in Eq. 8. By analogy to the logic underlying that VDI equation, the state diagram in Fig. 3 yields a closely similar expression for a standard measure of inactivation as given in Eq. 8:

$$CDI_{(V,F_U)} = \frac{J_{EFF}(V) \cdot X_{(V,F_U)}}{1 + J_{EFF}(V) \cdot X_{(V,F_U)}}, \tag{10A}$$

where

$$X_{(V,F_U)} = \frac{\Gamma}{\Gamma + 1} \cdot \frac{P_O(V) \cdot i(V)^2 \cdot F_U}{K_{D,EFF} + P_O(V) \cdot i(V)^2 \cdot F_U} \tag{10B}$$

The term X in Eq. 10 accounts for the voltage dependence of Ca^{2+} entry through the channel. In particular, for the context of Fig. 3 A, X equals the fractional occupancy of row 4, given residence in rows 1 through 4. This parameter then gives the fraction of noninactivated channels immediately poised for entry into the inactivated states within row 5. By inspection of Eq. 10B, it can be appreciated that X adheres to a Michaelis-Menten relationship, where $P_O \cdot i^2 \cdot F_U$ represents the amount of calcium driving the system, and $K_{D,EFF}$ is the effective Ca^{2+} dissociation constant of the CaM/channel complex. Substituting Eq. 10B into Eq. 10A, followed by algebraic simplification, yields an alternate but equivalent expression for *CDI:*

$$CDI_{(V,F_U)} = \frac{\hat{J}_{(V)}}{\hat{J}_{(V)} + 1} \cdot \frac{P_{O(V)} \cdot F_U}{K_{D,EFF}/[i_{(V)}^2 \cdot (\hat{J}_{(V)} + 1)] + P_{O(V)} \cdot F_U}, \tag{10C}$$

where $\hat{J}_{(V)} = J_{EFF(V)} \cdot \Gamma/(\Gamma + 1)$. Eq. 10 forms the basis of our upcoming analysis, wherein we extend our experimental determination of $J_{EFF}(V)$ to the CDI case, and establish equivalence of the full-blown CDI mechanism here (Fig. 3) to the simpler formalism used in our companion paper (Tadross et al., 2010), and to those in our previously published work (Tadross et al., 2008).

Mechanistic equivalence of CDI formalisms

The full-blown CDI state diagram in Fig. 3 A contains significantly more detail than the relatively simplified schemes used in our companion paper (Fig. 1, C and E, in Tadross et al., 2010) and our previously published work (Fig. 2 A of Tadross et al., 2008). Although the full-blown gating scheme of the present work furnishes a richer appreciation of the molecular features that potentially underlie CDI, all three formalisms are ultimately equivalent, as follows. For comparison of Eq. 10 to our previously published mechanism of CDI (Tadross et al., 2008), we recall that the main form of CDI for $Ca_V1.3$ channels was found to adhere to the following slow CaM relation (Eq. 1 in Tadross et al., 2008):

$$CDI_{(V = V_U, F_U)} = G \cdot \frac{P_O(V_U) \cdot F_U}{K_{eff} + P_O(V_U) \cdot F_U} \tag{11}$$

The condition $V = V_U$ reflects the fact that our previous work probed CDI at a single voltage V_U, but with a

variable degree of chop block ($0 < F_U < 1$). Notably, Eq. 11 (from our prior work) is of the same form as Eq. 10C of this work, and the two equations become identical given $V = V_U$ and:

$$G = \hat{J}_{(V_U)} / (\hat{J}_{(V_U)} + 1) \tag{12A}$$

and

$$K_{eff} = K_{D,EFF} / [i_{(V_U)}{}^2 \cdot (1 + \hat{J}_{(V_U)})] \tag{12B}$$

Thus, our previously published slow CaM mechanism is equivalent to the full-blown scheme in this present work.

In relation to our companion paper (Tadross et al., 2010), Eq. 10C can be seen as equivalent to Eq. 4 of that work. In particular, noting that $F_U = 1$ in our companion paper (given the use of standard depolarizations with no voltage block), and making the reasonable approximation $\hat{J}_{(V)} / (\hat{J}_{(V)} + 1) \sim 1$, such that CDI proceeds to near completion under saturating Ca^{2+}, Eq. 10C becomes

$$CDI_{(V)} \approx \frac{P_{O(V)}}{K_{D,EFF} / [i_{(V)}{}^2 \cdot (\hat{J}_{(V)} + 1)] \; + \; P_{O(V)}} \tag{13}$$

Eq. 13 thus corresponds precisely to Eq. 4 of our companion paper, where $K_{eff} = K_{D,EFF} / [i_{(V)}{}^2 \cdot (\hat{J}_{(V)} + 1)]$, in agreement with Eq. 12B. In all then, the dependence of CDI upon depolarization voltage, as well as on the degree of chop block, is equivalent among the CDI schemes in Fig. 3 here, those in our companion paper, and those in our previously published work (Tadross et al., 2008).

Determination of $J_{EFF}(V)$ for CDI

By analogy to our VDI analysis, a semiquantitative mapping of the state dependence of CDI relies upon our ability to derive an experimentally constrained analytic expression for $J_{EFF}(V)$. Eq. 10A furnishes a nearly direct relationship between *CDI* and J_{EFF}, except for an additional term *X*, which was absent within the VDI case seen in Eq. 8. Fortunately, all of the parameters underlying *X* (Eq. 10B) can be experimentally determined. First, $P_O(V)$ and $i(V)$ can be accurately determined from single-channel experiments (Tadross et al., 2008). Next, determination of $K_{D,EFF}$ can be deduced from previously determined values of *G* and K_{eff} in Eq. 11 (Tadross et al., 2008), as determined at a particular voltage, V_U. This is achieved by simple algebraic rearrangement of Eq. 12, which reveals that $\hat{J}_{(V_U)} = G / (1 - G)$ and thus:

$$K_{D,EFF} \; = \; \frac{K_{eff}}{(1-G)} \cdot i_{(V_U)}{}^2 \tag{14}$$

Hence, the effective Ca^{2+} dissociation constant of the CaM/channel complex ($K_{D,EFF}$) can be directly obtained from our previous voltage block experiments (Tadross et al., 2008). Although this determination of $K_{D,EFF}$ is based upon experiments performed at $V = V_U$, the expression for $K_{D,EFF}$ (Eq. 14) is notably independent of voltage. Thus, we can substitute the value of $K_{D,EFF}$ from Eq. 14 into our voltage-dependent expression for *X* (Eq. 10B) to yield:

$$X_{(V)} \; = \; \frac{\Gamma}{\Gamma + 1} \cdot \frac{P_{O(V)} \cdot i_{(V)}{}^2}{\frac{K_{eff}}{(1-G)} \cdot i_{(V_U)}{}^2 \; + \; P_{O(V)} \cdot i_{(V)}{}^2} \tag{15}$$

Note that we have now set $F_U = 1$ (for normal depolarizations). Recalling that $\Gamma / (\Gamma + 1) \sim 1$ for the usual CDI that achieves near completion, we arrive at a relationship (based on Eq. 10A) that constrains $J_{EFF}(V)$ in terms of experimentally determined entities:

$$J_{EFF(V)} = \frac{CDI_{(V)}}{1 - CDI_{(V)}} / \underbrace{\frac{P_{O(V)} \cdot i_{(V)}{}^2 \; / \; i_{(V_U)}{}^2}{\frac{K_{eff}}{(1-G)} \; + P_{O(V)} \cdot i_{(V)}{}^2 \; / \; i_{(V_U)}{}^2}}_{X(V)} \tag{16}$$

Eq. 16 thus allows us to calculate $J_{EFF}(V)$ for the CDI case. To summarize the methodology, determination of the state dependence of CDI via Eq. 16 requires an experimental measure of $CDI(V)$, single-channel ramp data to determine channel open probability ($P_O(V)$) and unitary current amplitude ($i(V)$) (Tadross et al., 2008), and whole cell voltage block experiments to determine the effective Ca^{2+} dissociation constant of the CaM/channel complex ($K_{eff}/(1\text{-}G)$) (Tadross et al., 2008).

Specific implications of CDI analysis for end-point mechanisms of CDI

Beyond determining the state dependence of entry into CDI, this methodology has further specific relevance to key deductions of our companion paper (Tadross et al., 2010). To articulate this connection, let us briefly summarize how our companion paper examines the end-point mechanisms of CDI. There, we argue that data from an S6 mutagenesis scan distinguishes in favor of an allosteric, rather than hinged-lid or pore collapse, CDI mechanism. Importantly, the ability to distinguish between these differing mechanisms relies upon a conceptually simple formulation of F_{CDI}, defined in our companion paper as the fraction of channels that are inactivated at steady state (compare with Figs. 1, C–F, of Tadross et al., 2010). For reference, F_{CDI} equals *CDI* if inactivated channels are electrically silent, whereas *CDI* would undershoot F_{CDI} if inactivated channels open sparsely (as in an allosteric CDI mechanism) (Tadross et al., 2010). In our companion paper, we assume that F_{CDI} depends only upon Ca^{2+} entry through the channel and

not upon state occupancy along the activation pathway. Given this assumption, F_{CDI} would attain a value near unity for S6 mutations that strongly enhance Ca^{2+} entry through the channel and monotonically decline for mutations that diminish Ca^{2+} entry. Critically, however, if this presumed monotonic decline of F_{CDI} were invalid, as might be the case if inactivation were to proceed preferentially from certain states along the activation pathway, the deductions in our companion paper could become ambiguous.

Fortunately, the methodology in this work allows us to explicitly analyze the factors underlying F_{CDI} and to ultimately confirm the relationship between F_{CDI} and mutation-induced perturbation of channel activation presumed in our companion paper. In this spirit, Fig. 4 displays three instructive channel gating schemes, nearly identical to those presented in Fig. 1 (D, 1, to F), except here an additional Ca^{2+}-driven step is included. In Fig. 4 (A, 1), inactivation proceeds exclusively from the open state. As in the VDI case, $J_{EFF}(V)$ rises with increasing voltage (blue curve in Fig. 4 A, 2), mirroring $P_O(V)$ (dashed curve). If we now fix $V = 0$, the effects of S6 mutations can be simulated by varying parameter 'a,' which scales the final activation transition (L in Fig. 4 A, 1). In this regimen, we can observe the dependence of F_{CDI} upon $\Delta\Delta G_a = -R \cdot T \cdot \ln(a)$, the mutation-induced change in the free energy of channel activation (Tadross et al., 2010). Specifically, then, we can recast Eq. 10A as:

$$F_{CDI(\Delta\Delta G_a)} = \frac{J_{EFF(\Delta\Delta G_a)} \cdot X_{(\Delta\Delta G_a)}}{1 + J_{EFF(\Delta\Delta G_a)} \cdot X_{(\Delta\Delta G_a)}}, \quad (17)$$

where the $\Delta\Delta G_a$ dependence of Eq. 17 arises from altered versions of Eqs. 1 and 2, in which $L(V)$ is scaled by parameter a. Fig. 4 A (3) shows the $\Delta\Delta G_a$ dependence of F_{CDI} and its underlying components, X and J_{EFF}. Thus, for the preferential open-state inactivation scheme of Fig. 4 A (1), all three terms decline as channel opening is diminished by mutation ($\Delta\Delta G_a > 0$), according to the presumptions of our companion paper. X decreases because a drop in P_O reduces average Ca^{2+} entry; J_{EFF} also

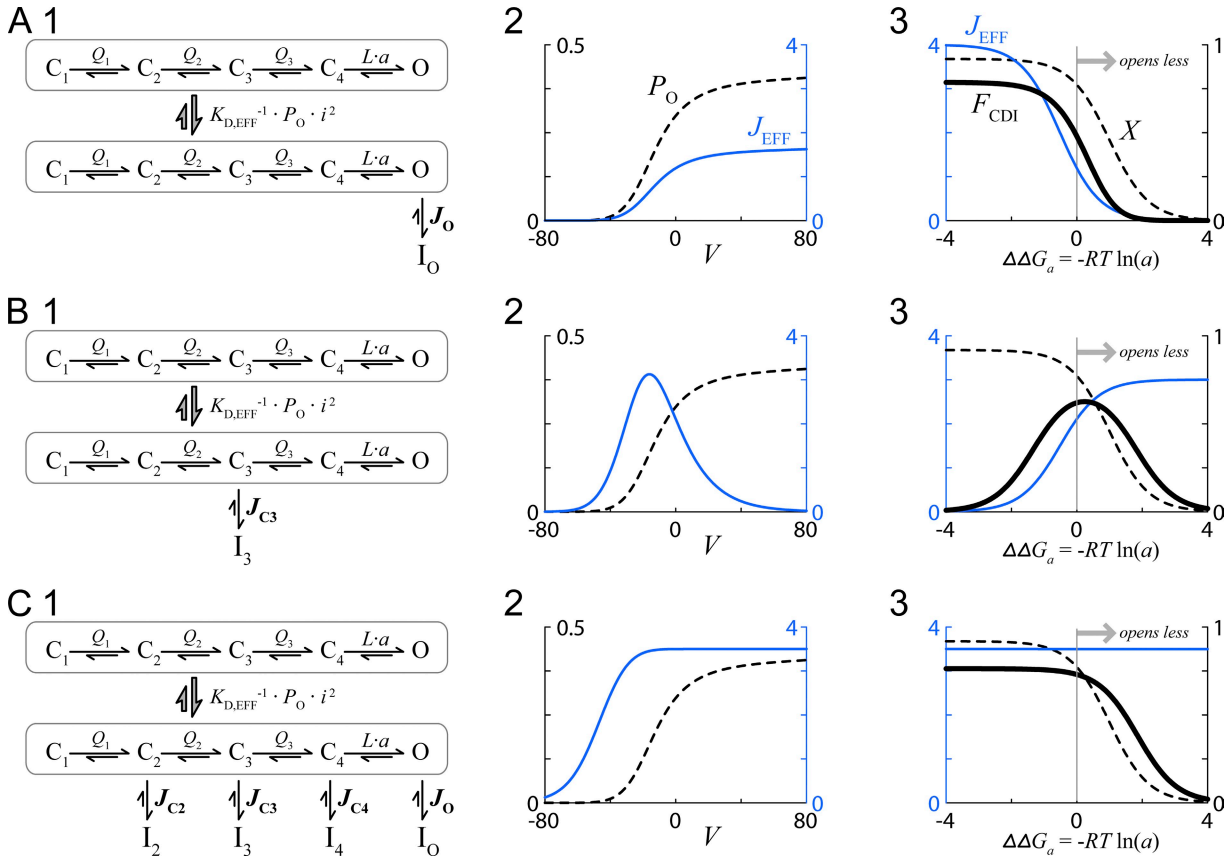

Figure 4. Tests for preferred states leading to CDI. (A) Behavior of the model in Fig. 3 if inactivation were to proceed exclusively from the open conformation. (A, 1 and 2) Analogous to Fig. 1 D. (A, 3) F_{CDI} and its underlying components J_{EFF} and X (Eq. 17), all at fixed voltage $V = 0$ with varying $\Delta\Delta G_a$, where $\Delta\Delta G_a = -R \cdot T \cdot \ln(a)$ and $R \cdot T = 0.6$ kCal/mole. The majority of parameters, including $Q_1(V)$, $Q_2(V)$, $Q_3(V)$, $L(V)$, J_{C1}, J_{C2}, J_{C3}, J_{C4}, and J_O, are all identical to those in Fig. 1 D. Beyond this, $G = 0.75$, $K_{eff} = 0.028$, and $i(V = 0)^2 / i(V_U)^2 = 1.27$. (B) Behavior of the model in Fig. 3 if inactivation were to proceed exclusively from state C_3. Format and parameters identical to A, except $J_{C1} = J_{C2} = J_{C4} = J_O = 0$ and $J_{C3} = 12$. (C) Behavior of the model in Fig. 3 if inactivation were to proceed equally from states C_2, C_3, C_4, and O. Format and parameters as in A, except $J_{C1} = 0$ and $J_{C2} = J_{C3} = J_{C4} = J_O = 3.5$.

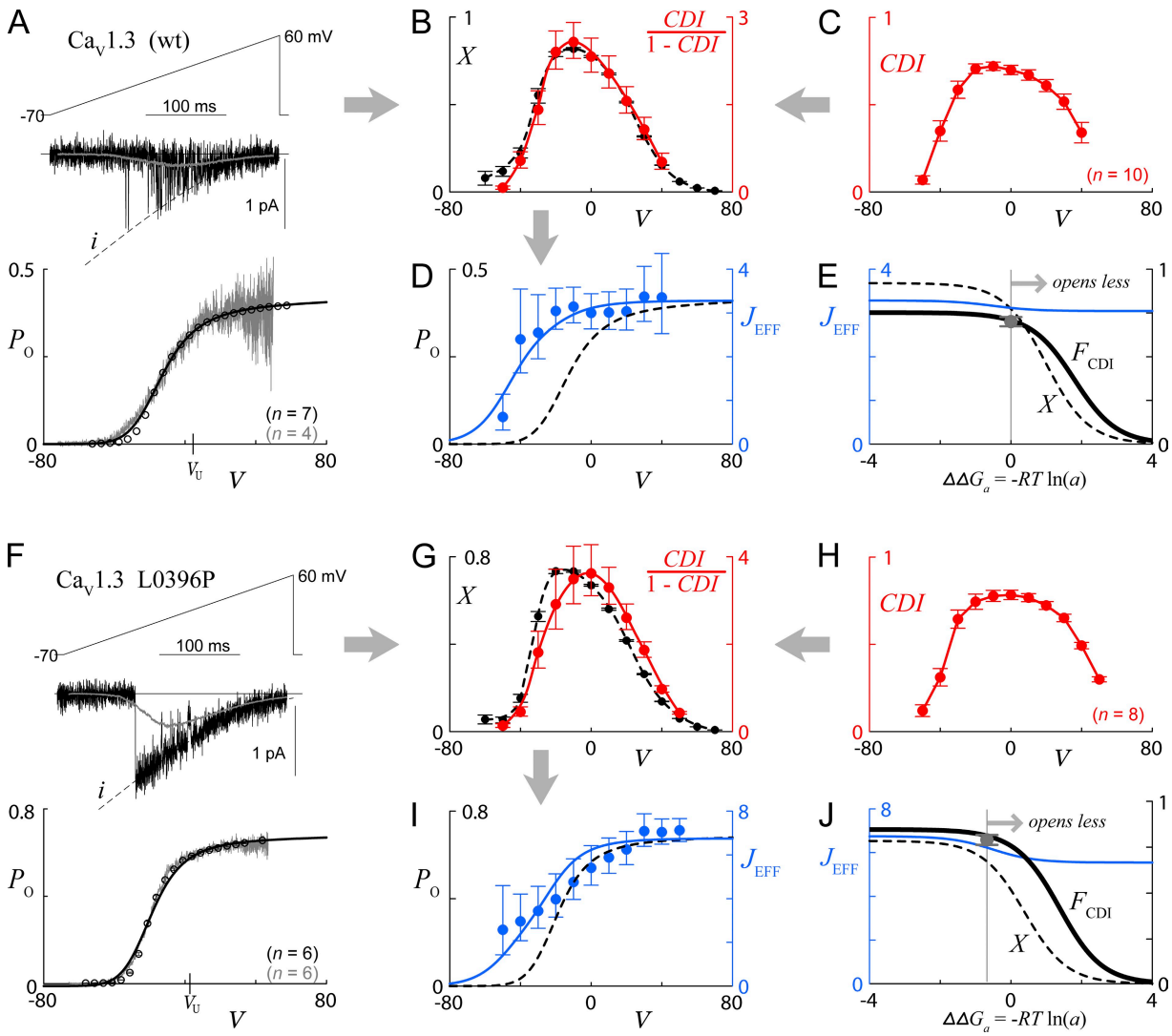

Figure 5. Actual tests for preferential closed state CDI. (A) Single-channel and tail-activation analysis of wild-type $Ca_V1.3$, reproduced from prior work (Tadross et al., 2008), after shifting along the voltage axis to account for different external solution used in the whole cell experiments of our companion paper (Tadross et al., 2010). Voltage is in units of mV throughout. (Top) Exemplar single-channel activity during voltage ramp protocol. Dashed black curve indicates the unitary current, $i(V)$. U-shaped gray curve (overlying exemplar trace) shows ensemble average current over many sweeps. Single-channel $P_O(V)$ curve (bottom) deduced by dividing ensemble average current into $i(V)$ relations. Circles represent whole cell tail activation data from prior work (Tadross et al., 2008). Number of cells (tail activation) and patches (single channel) are indicated in black and gray, respectively. Solid black curve overlying $P_O(V)$ corresponds to the model fit described below. See Tadross et al. (2008) for detailed experimental conditions and analysis methodology. (B) Components required for calculation of J_{EFF}. $X(V)$ (black) is deduced from Eq. 16, based upon $P_O(V)$ and $i(V)$ data in A, together with further voltage block parameters (Tadross et al., 2008) as follows: $G = 0.75$, $K_{eff} = 0.028$, and $i(V=0)^2/i(V_U)^2 = 1.27$. $CDI/(1 - CDI)$ in red is determined from data in C. (C) Population data for extent of CDI (CDI_{50} parameter from our companion paper, Tadross et al., 2010), plotted as a function of voltage. Error bars show SEM. Number of cells (n) as indicated. (D) $J_{EFF}(V)$ (blue symbols) calculated from the ratio of components in B, according to Eq. 16. Error bars represent the SEM, as estimated by transforming the mean ± SEM from experimental data via Eq. 16. Dashed black curve (replicated from P_O curve in A) and solid blue curve are based upon fits of the model in Fig. 4 C (1) to $P_O(V)$ and $J_{EFF}(V)$ data points. Parameters identical to Fig. 4 C, except $J_{C2} = J_{C3} = 2.55$ and $J_{C4} = J_O = 3.28$. (E) Predicted $\Delta\Delta G_a$ dependence of J_{EFF}, X, and F_{CDI} for the model fits described above, all at $V = 0$. Gray data point at $\Delta\Delta G_a = 0$ corresponds to CDI data point (at $V = 0$) from C, which closely approximates F_{CDI}. (F–J) Identical analysis as in A–E, here performed for the $Ca_V1.3$ L0396P mutant. Voltage block parameters for this channel are: $G = 0.83$, $K_{eff} = 0.051$, and $i(V=0)^2/i(V_U)^2 = 1.05$ (Tadross et al., 2008). Parameters for model fits in I and J are identical to those for the wild-type channel, except that $L(V)$ is multiplied by a factor of 3.1 (corresponding to $\Delta\Delta G_a = -0.68$ kcal/mole), and $J_{C2} = J_{C3} = 3.09$ and $J_{C4} = J_O = 6.75$. Model fits in J, as well as gray data point (corresponding to $V = 0$ data point from H), are shifted by −0.68 kcal/mole to reflect the enhanced opening of the $Ca_V1.3$ L0396P mutant.

decreases because a drop in P_O diminishes occupancy in the only state from which CDI can proceed (only $J_O \neq 0$). Both factors contribute to the monotonic decline of F_{CDI} with increasing $\Delta\Delta G_a$ (Fig. 4 A, 3). In contrast, in a second scenario where CDI proceeds far more readily from closed rather than open states, a very different

outcome can be observed (Fig. 4 B). Here, only J_{C3} is nonzero (Fig. 4 B, 1) yielding the hallmark bell-shaped $J_{EFF}(V)$ profile in Fig. 4 B (2) that mirrors occupancy within state C_3. Moreover, although P_O and X diminish with increasing $\Delta\Delta G_a$ (Fig. 4 B, 3, dashed relation), J_{EFF} actually increases with $\Delta\Delta G_a$ (Fig. 4 B, 3, blue curve), owing to enhanced state C_3 occupancy with attenuated opening. The combined effect of these opposing trends yields a bell-shaped F_{CDI}–$\Delta\Delta G_a$ relation (Fig. 4 B, 3). Notably, such an outcome could alone account for the principal experimental results of our companion paper (Fig. 4 A in Tadross et al., 2010), without postulating an allosteric mechanism (Fig. 1 F in Tadross et al., 2010). In a third possible scenario, inactivation proceeds equally from states C_2, C_3, C_4, and O (Fig. 4 C, 1), yielding the J_{EFF} profile in Fig. 4 C (2). As in the previous two cases, X declines with increasing $\Delta\Delta G_a$ because of the drop in P_O and thereby average Ca^2 (Fig. 4 C, 3, dashed curve). In contrast, J_{EFF} is now essentially independent of $\Delta\Delta G_a$ (blue curve) because inactivation can proceed equally well from open and several nearby closed states. As in the first scenario, F_{CDI} still declines with increasing $\Delta\Delta G_a$, but only due to the decline in Ca^{2+} entry (Fig. 4 C, 3). In all, only a configuration with preferential closed-state inactivation (Fig. 4 B) could undermine the deductions within our companion paper.

Application of analysis to the CDI of $Ca_V1.3$ channels

Thus armed with analytic insight, Fig. 5 shows the actual determination of J_{EFF} for the CDI process of wild-type $Ca_V1.3$ channels, as well as for the L0396P variant. These constructs were chosen because all their voltage block and single-channel parameters have been previously determined (Tadross et al., 2008), enabling use of Eq. 16. Fig. 5 A displays the single-channel data for the wild-type channel, as reproduced from prior work (Tadross et al., 2008), and Fig. 5 C shows the experimentally determined voltage dependence of *CDI* for this channel. These two datasets are transformed in Fig. 5 B to give the requisite components for J_{EFF} determination via Eq. 16, where $CDI/(1 - CDI)$ is in red, and X is in black. Taking the ratio of these yields J_{EFF} in Fig. 5 D (blue symbols), which is plotted along with the single-channel P_O relation (dashed black relation replicated from Fig. 5 A). From the monotonically rising shape of this experimentally determined $J_{EFF}(V)$, we conclude that CDI can proceed equally from both the open as well as some closed states near to the open state (compare with Fig. 4 C, 2). Although our experimentally derived determination of $J_{EFF}(V)$ does not require any explicit numerical modeling, for illustrative purposes, we fit the $P_O(V)$ and $J_{EFF}(V)$ data in Fig. 5 (A and D) to the model in Fig. 4 C (1), yielding the solid blue and dashed black curves in Fig. 5 D. The resulting parameters enabled us to simulate the F_{CDI}–$\Delta\Delta G_a$ relation in Fig. 5 E, which recapitulates the features of Fig. 4 C (3). Importantly, the data in Fig. 5 D could not be fit by a preferential closed-state model (e.g., Fig. 4 B) or an exclusive open-state inactivation scheme (Fig. 4 A). Thus, the curves in Fig. 5 E are well constrained by data in Fig. 5 D.

A similar analysis was performed on the L0396P mutant (Fig. 5, F–J). Again, the experimentally determined $J_{EFF}(V)$ relation (Fig. 5 I) corresponds well to a scenario in which CDI can proceed at least as well from the open, compared with several nearby closed, states. Reassuringly, only minor shifts in the details of the projected F_{CDI}–$\Delta\Delta G_a$ relations are apparent between wild-type and L0396P mutant (Fig. 5, E and J, solid black curves), consistent with the approximation that a single bell-shaped relation pertains to the suite of S6 mutations in our companion paper (Fig. 4 A in Tadross et al., 2010). Overall, in-depth analysis of the states from which inactivation occurs confirms the deductions of our companion paper, which argue that the end point of CDI involves an allosteric inhibition of activation gating.

Conclusion

This paper develops a systematic and straightforward approach for mapping the extent to which inactivation occurs from various states along the activation pathway, based only on open-channel measurements. The approach applies equally well to VDI and CDI, and emphasizes analytic manipulations of experimental data, rather than numerical simulations with numerous parameters. Additionally, our approach is applicable to the analysis of many other voltage-gated channels.

There are, however, certain limitations to the mapping strategy that warrant explicit consideration. Regarding VDI, the analysis assumes that activation proceeds more quickly than does inactivation. This assumption is usually true, but there are notable exceptions, such as with HERG voltage-gated K channels, where the relative speeds of inactivation and activation are reversed. In regard to CDI, our strategy requires that the off-rate of Ca^{2+} from CaM be slow, such that a slow CaM regimen holds true (Tadross et al., 2008). Other forms of CDI, such as an "SQS mechanism" in which Ca^{2+} unbinding from CaM is rapid (Tadross et al., 2008), may not be suitable for the analysis in this study.

With specific reference to inactivation properties of $Ca_V1.3$ channels, we detect very different state preferences for VDI and CDI. VDI is found to proceed almost exclusively from the open conformation (Figs. 1 D and 2). This propensity to inactivate only from the open state fits nicely with our homology models of open and closed conformations (Fig. 7 G in Tadross et al., 2010), in which the receptor for a hinged lid seems accessible only in the open but not closed state. In contrast, CDI transpires equally well from the open and nearby closed states, but is disfavored from deep closed states distant from the open conformation (Figs. 4 C and 5).

This stark contrast furnishes still further evidence that VDI and CDI are indeed distinct processes, a conclusion reached independently in our companion paper (Tadross et al., 2010). With specific regard to CDI, our analysis also demonstrates that the fraction of inactivated channels at steady state (F_{CDI}) bears a monotonic and roughly unique decline with increasing $\Delta\Delta G_a$, the change in free energy of channel activation produced by S6 mutations (Fig. 5, E and J). This outcome is critical to our companion paper, which assumed this result, in order to conclude that CDI ultimately represents an allosteric inhibition of activation gating. More broadly, numerous biological signaling pathways, including those controlling neuro-synaptic development (Krey and Dolmetsch, 2009), may be preferentially triggered by channels adopting specific conformations beyond the readily observable open state. As such, methodologies like those in this work may help to discern the state dependence of an expanding set of vital biological processes.

We thank Ivy Dick for her single-channel data in Tadross et al. (2008) and feedback on the manuscript, and Manu Ben Johny for helpful comments on the manuscript.

This work is supported by an Medical Scientist Training Program fellowship of the National Institute of General Medical Sciences (to M.R. Tadross) and by grant RO1MH065531 of the National Institute of Mental Health (to D.T. Yue).

Angus C. Nairn served as editor.

Submitted: 31 July 2009
Accepted: 15 January 2010

REFERENCES

Aldrich, R.W. 1981. Inactivation of voltage-gated delayed potassium current in molluscan neurons. A kinetic model. *Biophys. J.* 36:519–532. doi:10.1016/S0006-3495(81)84750-9

Aldrich, R.W., D.P. Corey, and C.F. Stevens. 1983. A reinterpretation of mammalian sodium channel gating based on single channel recording. *Nature.* 306:436–441. doi:10.1038/306436a0

Armstrong, C.M., and F. Bezanilla. 1977. Inactivation of the sodium channel. II. Gating current experiments. *J. Gen. Physiol.* 70:567–590. doi:10.1085/jgp.70.5.567

Bean, B.P. 1981. Sodium channel inactivation in the crayfish giant axon. Must channels open before inactivating? *Biophys. J.* 35:595–614. doi:10.1016/S0006-3495(81)84815-1

Bezanilla, F., and E. Stefani. 1994. Voltage-dependent gating of ionic channels. *Annu. Rev. Biophys. Biomol. Struct.* 23:819–846. doi:10.1146/annurev.bb.23.060194.004131

Brehm, P., and R. Eckert. 1978. Calcium entry leads to inactivation of calcium channel in *Paramecium*. *Science.* 202:1203–1206. doi:10.1126/science.103199

Cuello, L.G., J. Vishwanath, D.M. Cortes, A.C. Pan, D.G. Gagnon, J.F. Cordero-Morales, S. Chakrapani, B. Roux, and E. Perozo. 2009. Structural basis for the coupling between activation and inactivation gating in potassium channels. *Biophys. J.* 96:381a. doi:10.1016/j.bpj.2008.12.2852

Dunlap, K. 2007. Calcium channels are models of self-control. *J. Gen. Physiol.* 129:379–383. doi:10.1085/jgp.200709786

Evans, R.M., and G.W. Zamponi. 2006. Presynaptic Ca2+ channels—integration centers for neuronal signaling pathways. *Trends Neurosci.* 29:617–624. doi:10.1016/j.tins.2006.08.006

Hodgkin, A.L., and A.F. Huxley. 1952. A quantitative description of membrane current and its application to conduction and excitation in nerve. *J. Physiol.* 117:500–544.

Jones, L.P., C.D. DeMaria, and D.T. Yue. 1999. N-type calcium channel inactivation probed by gating-current analysis. *Biophys. J.* 76:2530–2552. doi:10.1016/S0006-3495(99)77407-2

Klemic, K.G., C.C. Shieh, G.E. Kirsch, and S.W. Jones. 1998. Inactivation of Kv2.1 potassium channels. *Biophys. J.* 74:1779–1789. doi:10.1016/S0006-3495(98)77888-9

Krey, J.F., and R. Dolmetsch. 2009. The Timothy Syndrome mutation in CaV1.2 causes dendritic retraction through calcium-independent activation of the Rhoa pathway. *Biophys. J.* 96:221a–222a. doi:10.1016/j.bpj.2008.12.1927

MacKinnon, R. 2003. Potassium channels. *FEBS Lett.* 555:62–65. doi:10.1016/S0014-5793(03)01104-9

Patil, P.G., D.L. Brody, and D.T. Yue. 1998. Preferential closed-state inactivation of neuronal calcium channels. *Neuron.* 20:1027–1038. doi:10.1016/S0896-6273(00)80483-3

Peterson, B.Z., J.S. Lee, J.G. Mulle, Y. Wang, M. de Leon, and D.T. Yue. 2000. Critical determinants of $Ca^{(2+)}$-dependent inactivation within an EF-hand motif of L-type $Ca^{(2+)}$ channels. *Biophys. J.* 78:1906–1920. doi:10.1016/S0006-3495(00)76739-7

Tadross, M.R., I.E. Dick, and D.T. Yue. 2008. Mechanism of local and global Ca2+ sensing by calmodulin in complex with a Ca2+ channel. *Cell.* 133:1228–1240. doi:10.1016/j.cell.2008.05.025

Tadross, M.R., M.B. Johny, and D.T. Yue. 2010. Molecular endpoints of Ca^{2+}/calmodulin- and voltage-dependent inactivation of $Ca_V1.3$ channels. *J. Gen. Physiol.* 135:197–215.

Thaler, C., A.C. Gray, and D. Lipscombe. 2004. Cumulative inactivation of N-type CaV2.2 calcium channels modified by alternative splicing. *Proc. Natl. Acad. Sci. USA.* 101:5675–5679. doi:10.1073/pnas.0303402101

Wu, L., C.S. Bauer, X.G. Zhen, C. Xie, and J. Yang. 2002. Dual regulation of voltage-gated calcium channels by PtdIns(4,5)P2. *Nature.* 419:947–952. doi:10.1038/nature01118

Xu, J., and L.G. Wu. 2005. The decrease in the presynaptic calcium current is a major cause of short-term depression at a calyx-type synapse. *Neuron.* 46:633–645. doi:10.1016/j.neuron.2005.03.024

Zagotta, W.N., T. Hoshi, J. Dittman, and R.W. Aldrich. 1994. Shaker potassium channel gating. II: transitions in the activation pathway. *J. Gen. Physiol.* 103:279–319. doi:10.1085/jgp.103.2.279